Original Article

Simultaneous Three-Dimensional Vascular and Tubular Imaging of Whole Mouse Kidneys With X-ray μCT

Willy Kuo[1,2,3] , Ngoc An Le[4] , Bernhard Spingler[4] , Roland H. Wenger[1,2] , Anja Kipar[5] , Udo Hetzel[6] , Georg Schulz[3] , Bert Müller[3,a] and Vartan Kurtcuoglu[1,2,7*,a]

[1]University of Zurich, Institute of Physiology, Winterthurerstrasse 190, 8057 Zurich, Switzerland; [2]University of Zurich, National Centre of Competence in Research, Kidney. CH, Winterthurerstrasse 190, 8057 Zurich, Switzerland; [3]University of Basel, Biomaterials Science Center, Department of Biomedical Engineering, Gewerbestrasse 14, 4123 Allschwil, Switzerland; [4]University of Zurich, Department of Chemistry, Winterthurerstrasse 190, 8057 Zurich, Switzerland; [5]University of Zurich, Laboratory for Animal Model Pathology (LAMP), Institute of Veterinary Pathology, Vetsuisse Faculty, Winterthurerstrasse 268, 8057 Zurich, Switzerland; [6]University of Zurich, Electron Microscopy Unit, Institute of Veterinary Pathology, Vetsuisse Faculty, Winterthurerstrasse 268, 8057 Zurich, Switzerland and [7]University of Zurich, Zurich Center for Integrative Human Physiology, 8057 Zurich, Switzerland

Abstract

Concurrent three-dimensional imaging of the renal vascular and tubular systems on the whole-kidney scale with capillary level resolution is labor-intensive and technically difficult. Approaches based on vascular corrosion casting and X-ray micro computed tomography (μCT), for example, suffer from vascular filling artifacts and necessitate imaging with an additional modality to acquire tubules. In this work, we report on a new sample preparation, image acquisition, and quantification protocol for simultaneous vascular and tubular μCT imaging of whole, uncorroded mouse kidneys. The protocol consists of vascular perfusion with the water-soluble, aldehyde-fixable, polymeric X-ray contrast agent XlinCA, followed by laboratory-source μCT imaging and structural analysis using the freely available Fiji/ImageJ software. We achieved consistent filling of the entire capillary bed and staining of the tubules in the cortex and outer medulla. After imaging at isotropic voxel sizes of 3.3 and 4.4 μm, we segmented vascular and tubular systems and quantified luminal volumes, surface areas, diffusion distances, and vessel path lengths. This protocol permits the analysis of vascular and tubular parameters with higher reliability than vascular corrosion casting, less labor than serial sectioning and leaves tissue intact for subsequent histological examination with light and electron microscopy.

Key words: computed tomography, contrast agents, kidney, tissue staining, vascular imaging

(Received 11 March 2020; revised 25 May 2020; accepted 5 June 2020)

Introduction

Renal function is dependent on the intricate three-dimensional (3D) arrangement of the kidney's vascular and tubular structures on both the local and whole-organ scales (Beeuwkes & Bonventre, 1975; Kriz, 1981; Pallone et al., 2003; Zhai et al., 2006; Bankir et al., 2020). Pathologies such as autosomal dominant polycystic kidney disease or fibrosis following acute kidney injury change the renal structure and may thereby affect the renal function beyond the primary disease mechanism (Wei et al., 2006; Tanaka & Nangaku, 2013; Venkatachalam et al., 2015). Whole-kidney imaging can be used to quantify structures and structural changes, yielding otherwise inaccessible entities such as whole-organ diffusion distances (Prommer et al., 2018), connectivity (Lantuejoul & Beucher, 1981), and distribution of compounds such as oxygen (Gardiner et al., 2011; Olgac & Kurtcuoglu, 2015, 2016; Kuo & Kurtcuoglu, 2017), both of which may be affected by pathologies.

The sampling of the entire organ is crucial when investigating phenotypes that are constricted to small, specific regions that may be overlooked in 2D sampling-based approaches (Hyde et al., 2007). However, concurrent whole-kidney imaging of vascular and tubular systems at capillary resolution is time-consuming, error-prone, and technically difficult.

Micro computed tomography (μCT) combined with vascular casting has been utilized in the evaluation of capillary rarefaction in ischemia–reperfusion, unilateral ureteral obstruction, and Alport models of kidney disease (Ehling et al., 2016), the measurement of vascular volume in different kidney regions (Garcia-Sanz et al., 1998), changes in kidney cortical vascular volume in a chronic bile duct ligation model of liver cirrhosis (Ortiz et al., 2000), the measurement of the vessel area of wrapped artery–vein pairs permitting oxygen shunting (Ngo et al., 2014), and in the analysis of blood vessel hierarchy and bifurcations (Nordsletten et al., 2006).

In vascular corrosion casting, polymerizing plastic resin is injected into the vasculature and the organ tissue is dissolved to yield a solid plastic cast that can be imaged with light or electron microscopy (Hossler & Douglas, 2001; Krucker et al., 2006; Wagner et al., 2006, 2011; Wei et al., 2006; Hossler et al., 2013). Since this approach destroys the tissue, the concurrent or subsequent analysis of renal tubules or other structures is impossible.

For corrosion-free vascular casting, plastic resins with radiopaque additives such as lead chromate, barium sulfate, or iodine compounds are available, permitting nondestructive imaging with X-ray µCT (Grabherr et al., 2008; Vasquez et al., 2011; Wagner et al., 2011; Haenssgen et al., 2014; Ehling et al., 2016; Perrien et al., 2016). Without such additives, vascular lumina or renal tubular tissue cannot be distinguished from water or agar background with standard laboratory X-ray source µCT.

As the plastic resins employed in vascular casting are hydrophobic, any water-based fluid present in the vasculature must be displaced physically during the injection. This requires well-optimized injection procedures combined with ligations to divert all resin flow to the organ of interest (Ghanavati et al., 2014). If water is incompletely removed, water inclusions can result in visible bubbles instead of fully filled large vessels (Vasquez et al., 2011; Ehling et al., 2016). To reduce this problem, flow rate and thus perfusion pressure are typically increased, which, in the kidney, may lead to bleeding into the renal capsule, visible as shape distortion of the kidney surface. Tubules may also collapse during perfusion with hydrophobic substances due to the lack of tubular counter pressure in the absence of glomerular filtration (Hlushchuk et al., 2018). These challenges make the preparation of an artifact-free sample technically difficult, frequently resulting in large numbers of samples with incomplete filling that have to be excluded from the respective study (Chugh et al., 2009; Fan et al., 2019).

To simplify the procedure of vascular imaging and allow for simultaneous acquisition of the cortical tubular network, we developed a new approach around XlinCA, an iodine-based contrast agent developed specifically for ex vivo X-ray µCT (Le et al., 2020). XlinCA is a water-soluble polymer large enough to avoid glomerular filtration. It can be crosslinked with glutaraldehyde to be retained within the vasculature permanently. As a water-soluble compound, the issue of water inclusions common to hydrophobic vascular casting resins is inherently avoided. Polymerization can be initiated from outside the organ at any time, obviating the need for the optimization of injection time. Perfusion with XlinCA can, therefore, proceed for as long as is required to achieve proper filling of the vasculature. Beyond resolving these artifacts, XlinCA features limited passive accumulation in the tubular walls in the cortex and outer medulla and enables the visualization of these features within the same µCT scan.

The protocol presented herein allows for imaging the renal vascular and tubular systems in 3D with a single µCT acquisition. In addition, it provides a simple step-by-step image processing and quantification workflow that requires no specialized image processing expertise and relies solely on the freely available Fiji/ImageJ software platform. Overall, it enables the quantification of vascular parameters with higher reliability than vascular corrosion casting, permits the analysis of tubular parameters with less labor than serial sectioning, and allows for subsequent histological and ultrastructural examination with light and electron microscopy.

Materials and Methods

Detailed methods, including chemical suppliers, surgical guide, detailed scan parameters, and exact image processing steps, are provided in Supplementary Data.

X-ray Contrast Agent Synthesis

The contrast agent was synthesized as described previously (Le et al., 2020). In brief, an acryloyl group was added to the amine of 5-amino-2,4,6-triiodoisophthalic acid. The resulting compound was polymerized via reversible addition–fragmentation chain-transfer polymerization (Chiefari et al., 1998; Lai et al., 2002) to a molecular weight of approximately 30,000 g/mol. Ethylenediamine was coupled with the carboxylic acid groups of the polymer to add free amine groups, enabling aldehyde fixation. The chemical structure of the compound is given in Supplementary Figure S1. To increase the size of the polymer, it was precrosslinked with a small amount of glutaraldehyde and dialyzed using a membrane with a cutoff of 100,000 g/mol.

Mouse Husbandry

Three female C57BL/6J mice were purchased from Charles River Laboratories and Janvier Labs and were kept until the age of 7 or 10 months in individually ventilated cages with *ad libitum* access to water and standard rodent food (Kliba Nafag 3436) in 12 h light/dark cycles. All animal experiments were approved by the veterinary office of the canton of Zurich (license number ZH233/15).

Abdominal Aorta Perfusion

The mice were anesthetized with ketamine/xylazine, and kidneys were perfused retrogradely via the abdominal aorta (Czogalla et al., 2016) with a 21 G butterfly needle connected via a 2.5 m long silicone tube to a reservoir providing 150 mmHg of hydrostatic pressure, which resulted in flow rates of about 5 mL/min. Kidneys were flushed with approximately 10 mL of phosphate-buffered saline (PBS) and fixed with 100 mL 4% formaldehyde/ 1% glutaraldehyde in PBS. Remaining aldehydes were flushed out with 20 mL of PBS and quenched with 50 mL of glycine solution (5 mg/mL in PBS), then flushed again with another 40 mL of PBS. All solutions used for perfusion were kept at 37°C.

4 mL of XlinCA contrast agent solution (75 mg iodine/mL) was perfused using a 10 mL syringe, actuated with a constant weight to provide 150 mmHg of pressure. Flow rates were typically between 0.3 and 0.5 mL/min. The abdominal cavity was then filled with 4% glutaraldehyde in PBS to crosslink the contrast agent, and the kidneys were removed afterwards and kept in 4% glutaraldehyde/PBS. These solutions were kept at room temperature.

Fixed kidneys were mounted in 1% agar in PBS in either standard 1.5 mL centrifugation tubes or 0.5 mL PCR tubes for scanning, depending on their size.

X-ray µCT Image Acquisition

The X-ray µCT data were acquired with a nanotom® m (phoenix| x-ray, GE Sensing & Inspection Technologies GmbH, Wunstorf, Germany), equipped with a tungsten target and diamond window. Acceleration voltage was set to 60 kV and current to 310 µA. 1440 projections were acquired per height step with a GE DXR detector with a 3072 × 2400 pixel array with 0.5 s exposure time. Kidneys mounted in 1.5 mL tubes were scanned with 4.4 µm isotropic voxel size. Three frames per projection were recorded and averaged, resulting in a scan time of approximately 3 h per kidney. The one kidney mounted in a 0.5 mL tube was scanned with 3.3 µm isotropic voxel size with 12 frames per projection averaged, resulting in 10 h of scan time. Four height steps were required for each kidney. Reconstruction was performed with the manufacturer's GE phoenix datos|x software.

Histological Examination

Fixed kidneys were trimmed (midline longitudinal or cross-section) and paraffin wax embedded. Consecutive sections (3–5 μm) were stained with hematoxylin-eosin (HE) and the periodic acid Schiff (PAS) reaction for histological examination, or were deparaffinized and left unstained for the assessment of fluorescence. Slides were photographed through a Nikon Eclipse Ni-U microscope equipped with a digital camera and scanned using a digital slide scanner with 40× magnification (NanoZoomer-XR C12000, Hamamatsu, Japan).

Transmission Electron Microscopy Examination

A slice of fixed kidney (midline cross-section) was trimmed and embedded in epoxy resin. Toluidine blue-stained semithin (1.5 μm) sections were prepared to select areas of interest for the preparation of ultrathin (75 nm) sections that were either directly viewed with a Philips CM10 microscope, operating with a Gatan Orius SC1000 digital camera (Gatan Microscopical Suite, Digital Micrograph), or were contrasted with lead citrate and uranyl acetate and viewed subsequently.

Example Segmentation and Quantification

The 3.3 μm dataset was segmented using the free Fiji/ImageJ software (Schindelin et al., 2012; Schneider et al., 2012) with the MorphoLibJ (Legland et al., 2016) and 3D ImageJ Suite plugins (Ollion et al., 2013) installed. A 3D Gauss filter with $\sigma = 1$ pixel was applied, and the blood vessel lumina were extracted by setting manual thresholds. A rough kidney mask was created with a lower threshold, then erosion and connected component analysis with the MorphoLibJ plugin (Legland et al., 2016) were used to remove areas of contrast outside the kidney. This mask was then applied to the blood vessel segment.

The blood vessel segment was transformed into a more refined kidney mask by dilation, 3D hole filling using the 3D ImageJ Suite plugin (Ollion et al., 2013) and subsequent erosion. This mask was combined with thresholding of the water background to obtain the tubular lumina. Any remaining volume within the mask that was part of neither the blood vessels nor the tubular lumina was declared kidney tissue. The binary representations of the segmented vascular lumina, tubular lumina, and kidney tissue are available together with the original μCT dataset on the *Zenodo* public repository, doi: 10.5281/zenodo.3354338.

Blood vessel and tubular volumes were calculated by adding up the number of voxels in the binary segments. The blood vessel and tubuli surface areas were estimated with the MorphoLibJ plugin by counting the number of line probe intersections in 13 different directions. A marker point was manually selected at the papilla of the kidney in the blood vessel segment, and the geodesic distance map was calculated using the same plugin. The Euclidean distance map and all histograms were calculated using default Fiji/ImageJ functions.

Image processing was performed on a workstation equipped with 256 GB RAM and two 8-core Intel Xeon E5-2670 processors. 3D computer graphic images of the segmentation were rendered with Arivis4D 2.12.4 (Arivis, Germany) on a virtual machine with 174 GB of RAM, 7 Intel Xeon E5-2680 v2 cores, and pass-through Nvidia GRID K2 graphics.

Results

Vascular casting of mouse kidneys with the water-soluble, cross-linkable contrast agent XlinCA was carried out at a fixed perfusion pressure without the need to maintain a minimum flow rate. No water inclusions or disconnected vessels could be identified, even in kidneys perfused at low flow rates that would result in severe filling artifacts with conventional plastic resin-based vascular casting materials.

μCT datasets of six mouse kidneys were acquired with 4.4 μm voxel size and sufficient contrast to distinguish vascular and tubular lumina, as is shown in Figure 1 using both the original grayscale and a false-color map mimicking the appearance of HE-stained histological sections. Contrast retention within the vascular lumen and cortical tubular tissue was permanent. One additional dataset with 3.3 μm voxel size was acquired after 1 month of storage and did not exhibit any reduction in contrast between blood vessels, surrounding tissue, and background.

Fluid-filled longitudinal structures in the inner stripe of the outer medulla could be identified in the μCT data in all mice, despite using healthy mice with nontransgenic background and without any intervention (Supplementary Fig. S2). These structures would not have been captured with previous vascular casting methods, which provide no direct means of identifying specific structures in the tissue. The histological examination shown in Figure 2 identified those as protein casts within thin ascending tubules, and the PAS reaction confirmed that, unlike the contrast agent, these casts contained some polysaccharides. There was no histological evidence of tissue damage. The latter was confirmed also at the ultrastructural level. Cellular ultrastructures were well preserved in transmission electron microscopy images (Supplementary Fig. S3). Capillaries were found to be well filled with the contrast agent and their diameter increased compared to unperfused kidneys, although the change in capillary diameter is too small to be captured by μCT with 3.3 μm wide voxels. The increase is a consequence of the 150 mmHg of perfusion pressure employed during fixation, which was chosen to increase the reliability of the initial flushing step to remove blood. While this is well above resting blood pressure, it represents the upper end of blood pressure during physical activity (Adlam et al., 2011; Burgess et al., 2019) and is in keeping with or lower than perfusion pressures typically used in vascular casting (Chugh et al., 2009; Ghanavati et al., 2014; Epah et al., 2018).

Tubular lumina were also found to be slightly dilated, featuring diameters in the range of 20–40 μm compared with the *in vivo* situation where tubular diameters are closer to 20–30 μm in mice (Hall et al., 2013). This deviation lies within the variability of other sample preparation methods and other factors such as the choice of anesthetic *in vivo*.

To determine the contrast agent behavior under suboptimal conditions, a kidney with incomplete perfusion due to surgical mistakes was evaluated. The presence of erythrocytes in blood vessels not filled with contrast agent (Supplementary Fig. S4) suggests that the lack of filling is caused by insufficient flushing of the blood vessels prior to contrast agent injection. It is thus not an issue directly related to the agent. Filling with contrast agent is likely primarily dependent on the quality of the initial blood removal step.

The quality of the μCT data with a voxel size of 3.3 μm enabled us to extract the vascular and tubular lumina of a single kidney as binary masks using a semiautomatic workflow in Fiji/ImageJ, and to visualize them with Arivis4D as shown in Figure 3 and the
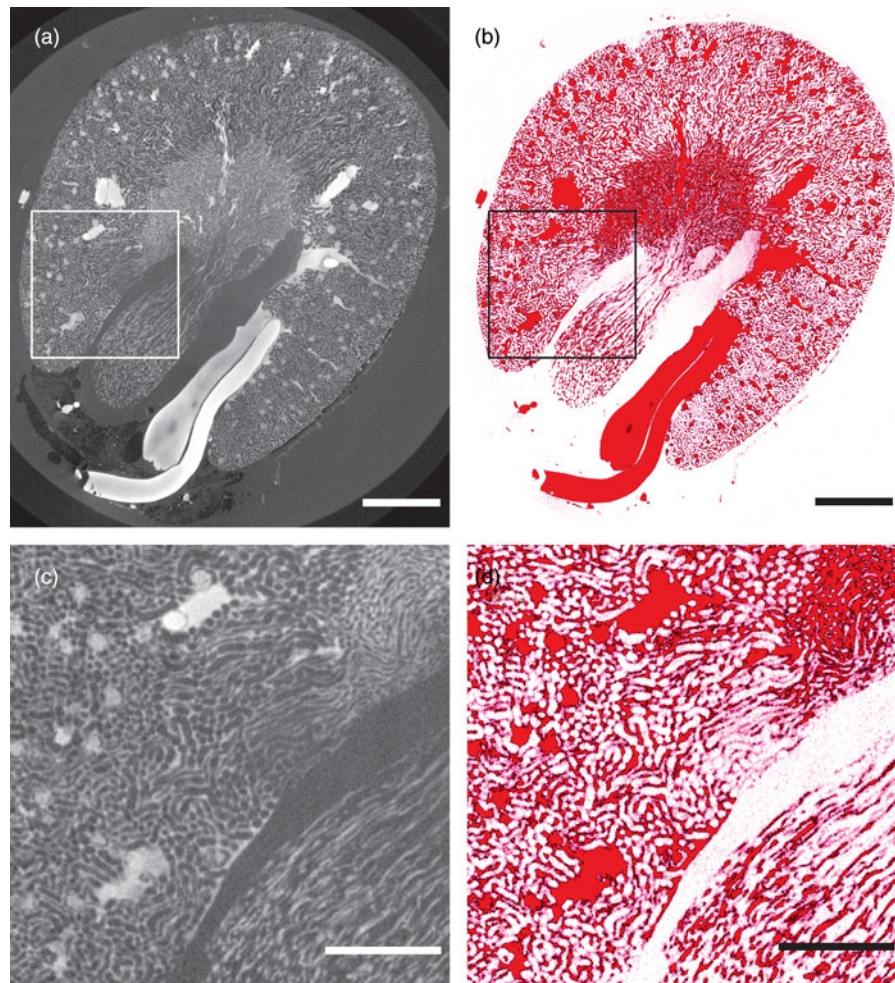
Fig. 1. (**a**) Virtual section of the 3.3 μm voxel size μCT dataset displaying blood vessels (white and light gray) and tubular walls (gray). (**b**) False-color image of the same virtual section of the μCT dataset, approximating the appearance of a HE-stained histological section. Red: blood vessels, purple: tubular walls. Scale bars: 1 mm. (**c,d**) Magnified views of the boxed regions in the top panels containing parts of the cortex, outer medulla, and inner medulla. Scale bars: 0.5 mm.

Supplementary Video available on the *Zenodo* public repository, doi: 10.5281/zenodo.3354338. These segmented 3D data can be employed to determine quantities such as blood vessel density —a measure used to quantitatively characterize capillary rarefaction (Ehling et al., 2016)—by computing the number of voxels of the masks with standard Fiji/ImageJ functions. This approach is mathematically identical to the point probe intersection method used in the stereological quantification of histological sections. The volume of the segmented blood vessel lumina was 65.6 mm^3, of the tubular lumina 58.5 mm^3, of the tissue 42.6 mm^3, and of the whole kidney 166.7 mm^3, resulting in a vessel density of 39%. While this value is considerably higher than 25.1% Garcia-Sanz et al. (1998) calculated based on rat kidney vascular casts, their dataset was unable to fully resolve capillaries, and vascular density was, therefore, estimated by assuming a linear relationship between vessel density and mean gray value of the kidney. We expect our measurement to be the more accurate one, as capillaries were identified explicitly, could be validated visually and the discrepancy is consistent with similar underestimation of vascular density based on under-resolved μCT images (Epah et al., 2018).

Line probe intersection can be used in the stereological quantification of histological sections to measure surface area. Instead

of using a counting frame, we applied it to the binary masks in a fully automatic manner using MorphoLibJ. Surface areas were 8433 and 8775 mm^2 for the segmented blood vessels and tubules, respectively. This information can be used, for example, to quantify the diffusion of oxygen across the blood vessel walls, which is proportional to the surface area (Ngo et al., 2014). We are certain to have underestimated total surface area: Some vessels, such as the glomerular capillaries or vessels of the vascular bundles, are located too close together to be distinguished at the given resolution. The numbers reported represent, therefore, a lower limit. They are also usable for the comparative quantification of datasets with identical resolution.

The 3D Euclidean distance of each voxel to the nearest blood vessel was calculated. This represents the minimal diffusion distance of a given location of the kidney to the nearest source of oxygen and nutrients (Borgefors, 1996) and can be used to quantify the amount of tissue that is insufficiently supplied (Prommer et al., 2018). The 3D Euclidean distance was determined for the entire space of the kidney devoid of blood vessels, creating a map as shown in Figure 4a. We also evaluated the distribution of the distances within the kidney accounting for either the whole nonblood vessel space or only the renal tissue (Fig. 4c). 43% of the considered nonblood vessel space is contained within
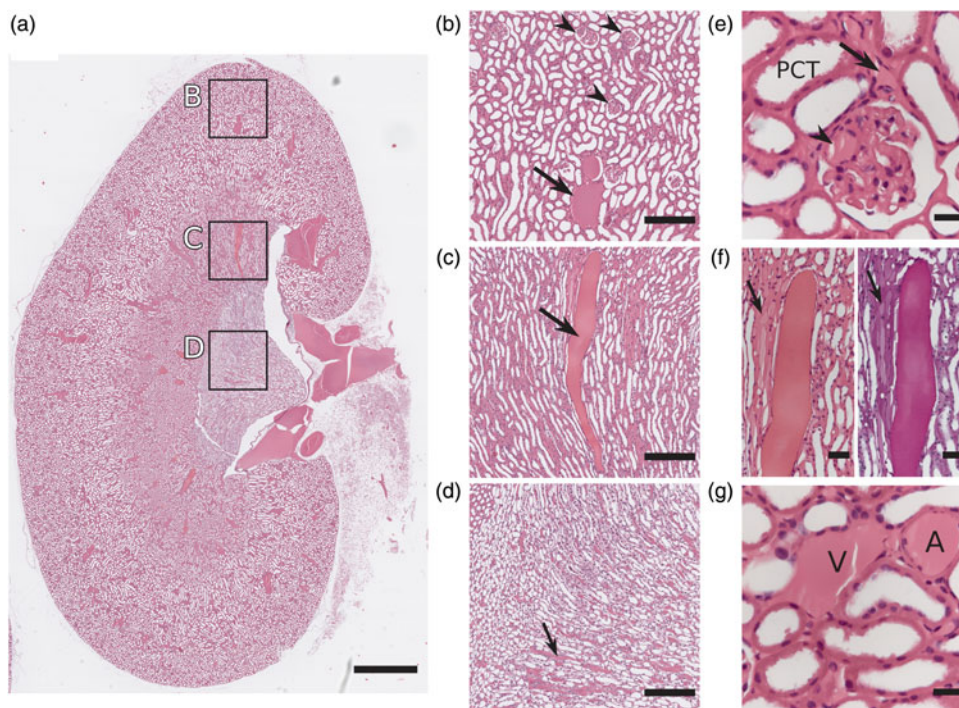
Fig. 2. Long-axis midline section of mouse kidney after perfusion with the contrast agent; HE stain. (**a**) Overview. Scale bar: 1 mm. (**b**) Part of renal cortex, containing glomeruli (arrowhead) and an artery–vein pair. The contrast agent is visible as homogenous, amorphous material that is eosinophilic due to the abundance of primary amine groups in its structure (arrow). Scale bar: 200 μm. (**c**) Inner stripe of the outer medulla, with one longitudinally cut tubule filled with an eosinophilic protein cast (arrow). Scale bar: 200 μm. (**d**) Inner medulla, containing contrast agent-filled vasa recta (arrow). Scale bar: 200 μm. (**e**) Cortex with glomerulus and proximal convoluted tubules. The contrast agent is seen within glomerular capillaries (arrowhead) and interstitial blood vessels (arrow). Scale bar: 20 μm. (**f**) Closer view of tubule in Figure 2c, filled with protein cast. Adjacent blood vessels contain the contrast agent (arrow). Left: HE stain; right: PAS reaction. Scale bars: 40 μm. (**g**) The contrast agent in an artery (A) and a vein (V) in the cortex. Scale bar: 20 μm.
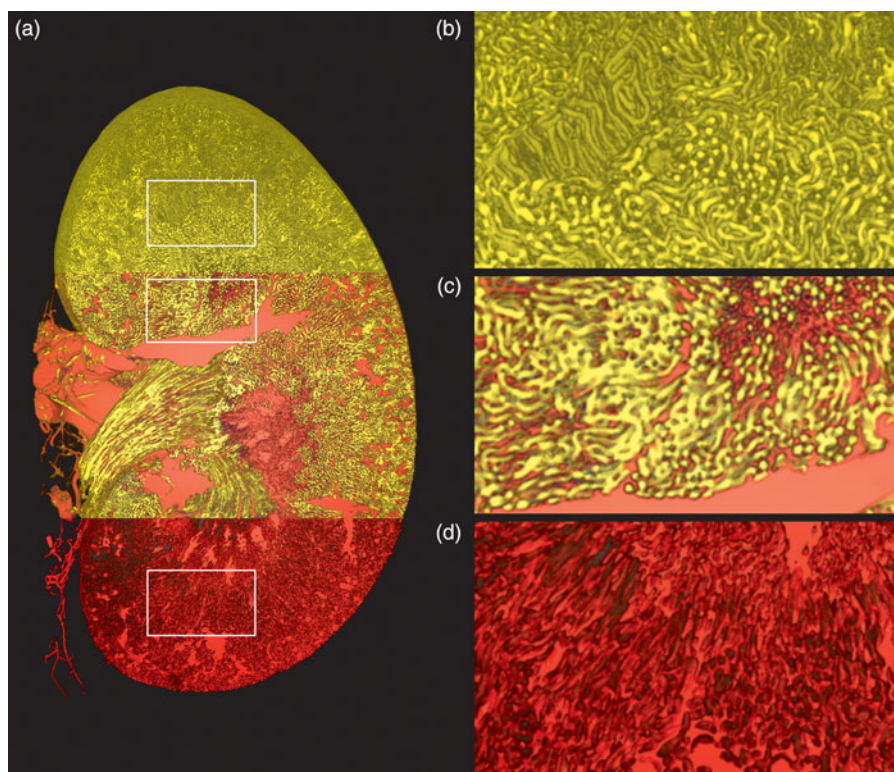
Fig. 3. Computer rendering of the vascular and tubular structures segmented from the μCT dataset with 3.3 μm voxel size. (**a**) Overview image including rectangles indicating the origin of the regions of interest shown on the right with higher magnification. In the top section, only tubular lumina (yellow) are displayed. Vascular lumina (red) are shown in the bottom section, and both segments are shown in the middle section. Height of the kidney: 10.3 mm. (**b**) Magnified view of segmented tubular lumina. (**c**) Magnified view of both tubular and vascular lumina. (**d**) Magnified view of segmented vascular lumina.
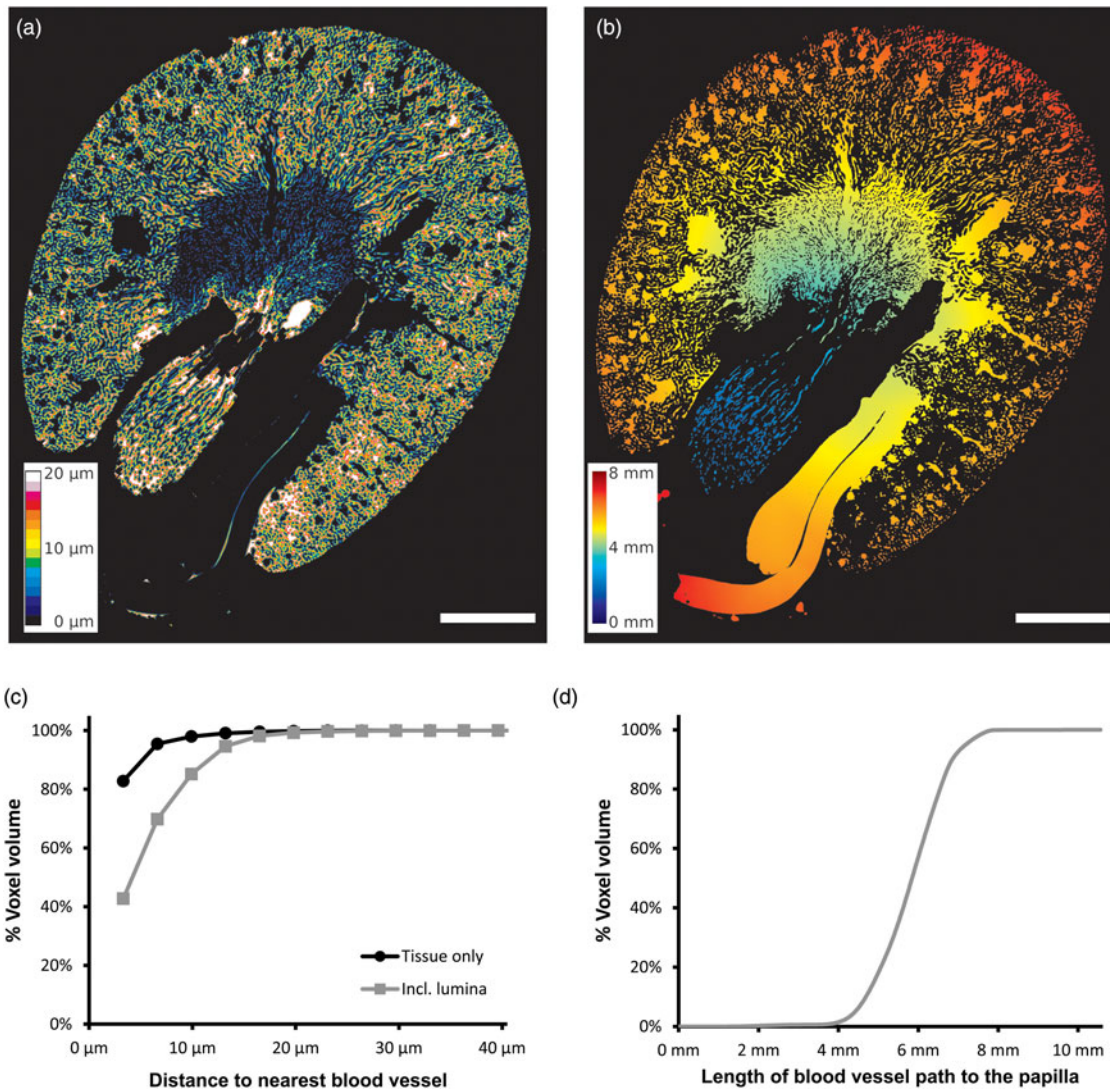
Fig. 4. (**a**) A kidney virtual section showing the diffusion distance of each voxel within the kidney to the nearest blood vessel. (**b**) Virtual section displaying the lengths of the shortest paths along blood vessels of each voxel to the papilla of the kidney. Scale bars: 1 mm. (**c**) Cumulative distribution function of the diffusion distances. (**d**) Cumulative distribution function of the blood vessel path lengths to the papilla.

the first neighboring voxel adjacent to a blood vessel if the whole space, including tubular lumina, is evaluated. However, if tubular lumina are excluded and only tissue is considered, 83% of the tissue is contained within the first voxel. This result demonstrates the potential for misinterpretation when evaluating the diffusion distances of oxygen or nutrients based solely on vascular data.

To illustrate the potential of 3D data for blood vessel path analysis, which is a measure inaccessible to 2D analysis, an arbitrary marker point in the blood vessel segment of the papilla was set and the lengths of the shortest path along the vasculature from every voxel to that marker were calculated. The resulting false-color map shown in Figure 4b indicates 4 mm path length as the cutoff distance at which the blood vessels exit the inner and enter the outer medulla. Calculating the cumulative distribution function revealed that only 1.5% of the blood vessel volume is contained in the inner medulla (Fig. 4d). In principle, this quantification method allows determining the length of any blood vessel or tubule (Lantuejoul & Beucher, 1981), provided that the image resolution is sufficiently high to avoid artificial shortcuts.

Discussion

Advantages in Vascular Imaging Over Previous High-Resolution CT Protocols

Our protocol represents an orthogonal approach to reducing artifacts encountered in 3D renal vascular imaging. We made use of a water-soluble contrast agent, XlinCA, to circumvent the problem of water inclusions caused by vascular casting with hydrophobic plastic resins. XlinCA features low viscosity and flow resistance, and polymerization can be initiated from outside the organ independent of the perfusion. This contrasts with vascular casting resins, for which polymerization and perfusion are not independent: Perfusion must be concluded within a fixed time frame—typically 20 min—before the resin is polymerized. Since perfusion with a minimum volume of resin is required to flush out all residual water inclusions, a certain minimum flow rate has to be ensured. As higher flow rates require higher perfusion pressures, the casting process must be optimized to achieve the required minimum flow rate without exceeding the maximum permissible perfusion pressure.

Since XlinCA only solidifies after the addition of glutaraldehyde, there is no upper time limit on how long an organ perfusion may proceed. Correspondingly, flow rate does not need to be optimized, and it does not need to be taken into consideration for optimizing perfusion pressure. These properties allowed us to achieve reliable filling of the renal vasculature with a higher success rate than using plastic-based vascular casting while requiring little optimization of parameters such as flow rate, perfusion pressure, and polymerization time.

The histologic examination revealed microscopic gas bubbles in the polymerized contrast agent hydrogel. These bubbles were invisible in the μCT datasets, since they were typically below the resolution limit and of much smaller size than the gas bubbles common in plastic resin-based vascular casting. It is, therefore, unclear whether these bubbles were present during the crosslinking of the contrast agent or were introduced only later during the processing steps required for the histologic examination. As a precaution, the contrast agent solution should be degassed extensively prior to perfusion if higher resolution scans are foreseen.

Standard clinical angiography contrast agents are water-soluble compounds unsuitable for high-resolution *ex vivo* vascular imaging since these low molecular weight compounds can pass through the blood vessel walls within minutes. They are furthermore cleared via glomerular filtration. While this is necessary to prevent their accumulation in patients' bodies, it also introduces the contrast agent into the tubular lumina, preventing a clear distinction between vascular and tubular structures (Lusic & Grinstaff, 2013). Blood pool contrast agents are designed for longer circulation times, and surface-functionalized metal nanoparticles are available in sizes that avoid glomerular filtration. However, in *ex vivo* settings, they tend to sediment, aggregate, and diffuse out of the vasculature, making them often unsuitable for capillary imaging in the kidney (Grabherr et al., 2007).

To resolve these issues encountered with water-soluble X-ray angiography contrast agents when used for high-resolution *ex vivo* imaging, XlinCA was designed as a polymeric compound with sufficiently large molecular weight to avoid extravasation or glomerular filtration. As a polymer of a 5-amino-2,4,6-triiodoisophthalic acid-derived monomer, the iodine content of 49.5% is considerably higher than contrast agents that rely on increasing their molecular weight by linkage to large molecules such as polyethylene glycol (Jin & Lu, 2014). Free amine groups allow for covalent crosslinking with glutaraldehyde, resulting in a sample with stable contrast for months or longer.

Tubular Imaging With Laboratory-Based μCT in Absorption Contrast Mode

The most important advantage of the protocol lies in the ability to image tubular walls in the cortex and outer medulla concurrently with the vasculature in the same μCT scan. This is contrary to conventional casting protocols where the contrast agent only labels the vascular lumina, leaving the native tissue essentially invisible for conventional μCT. We hypothesize that limited diffusion of the polydisperse XlinCA contrast agent into the tubular walls and fixation by unquenched aldehydes within the intracellular space of the tubules is responsible for this behavior. This interpretation is supported by the electron microscopy images, where no contrast agent could be found in Bowman's space or tubular lumen, and no aggregation was observed in the extracellular space.

The exact mechanism by which XlinCA accumulates in the tubular walls is unclear. Active uptake mechanisms can be excluded, since XlinCA is perfused only after extensive aldehyde fixation of the organ. The polymer is too large to pass through channels such as aquaporins, and the presence of large amounts of small molecule fractions can be excluded due to the lack of the contrast agent in Bowman's space. Passage through fenestrated epithelial layers would leave contrast agent in the extracellular space. Embedment of the hydrophobic parts of XlinCA in the lipid bilayer is unlikely, since the inner medulla is not stained.

While the exact mechanism of XlinCA accumulation in the tubular walls remains to be determined, tubular lumina and interstitial space remain free of the contrast agent. Tubular walls contain small concentrations and vascular lumina large concentrations of XlinCA, permitting concurrent imaging of these features in a single μCT scan. The tubular structure can thus be obtained without requiring subsequent serial sectioning, which is highly labor-intensive and may suffer from various sample preparation artifacts, notably shrinkage during dehydration and damage to the sections during sample handling. These artifacts complicate realignment and virtual reassembly of the sections, requiring nonrigid registration algorithms if structural data need to be preserved (Roberts et al., 2012).

The importance of visualizing tubules along with the vasculature must be emphasized: The amount of tissue in direct contact with blood vessels is underestimated by about 50% if the tubular lumen is not taken into account when determining the distribution of diffusion distances (Fig. 4c). Tubules provide important context when investigating the effect of renal diseases on the vasculature. Here, kidneys of aged mice featured areas not perfused by the vasculature, which could have been interpreted erroneously as signs of capillary rarefaction. With tubular imaging, we were able to identify those regions as liquid-filled structures instead, which were confirmed by histology to be eosinophilic protein casts, a common finding in healthy, aged mice.

Comparison to 3D Light Microscopy

3D imaging with microscopy on the whole-organ scale has been made possible in recent years via the introduction of tissue clearing, allowing for light-sheet microscopy on intact, uncut tissue by reducing light scattering via, for example, refractive index matching or lipid removal (Richardson & Lichtman, 2015). However, residual light scattering reduces the achievable resolution at depth and leads to optical distortion. In addition, the clearing process typically introduces swelling or shrinkage of the sample by 20% by length (Kolesova et al., 2016). Tissue clearing with light-sheet microscopy is, therefore, well suited for large, well-separated features at the renal surface, such as glomeruli (Yang et al., 2014; Klingberg et al., 2017), but not for capturing the dense capillary network in the deeper regions of the kidney.

Compared with visible light, X-rays penetrate soft tissue with negligible absorption and refraction, which allows X-ray μCT to provide 3D data with isotropic quality and resolution regardless of depth within the sample. Organs can be imaged fully intact in their hydrated state, preventing any further sample distortion beyond the minor volume changes introduced by fixation (Stowell, 2009; Tran et al., 2015). X-ray absorption is furthermore not dependent on chemically labile fluorescence reporters and does not incur any photobleaching. Samples can be imaged repeatedly at high photon fluxes with no contrast degradation, enabling hierarchical imaging.

Image Quality Was Achieved With a Previous-Generation X-ray μCT Scanner

The nanotom® m employed in this study uses a water-cooled tungsten target and a scintillator-coupled flat panel detector,

which is representative of advanced μCT scanners introduced almost a decade ago. Accordingly, the image quality presented in this work is achievable by a wide base of currently installed hard X-ray μCT systems and thus accessible to many research labs. Higher resolution and better image quality may be required if segmentation with higher precision is needed for a specific study. As samples do not degrade upon repeated measurements, they can be imaged with more expensive laboratory or synchrotron radiation-based μCT instrumentation if such a need is identified. The results presented in this work, therefore, do not represent the upper limits of the protocol, but rather a baseline that should be achievable by most existing μCT devices.

Simple Segmentation Based on Fiji/ImageJ

The presented image segmentation workflow is simple, relies solely on freely available software, and can be implemented without specialized knowledge in image processing or programming (see Supplementary Methods). To segment larger numbers of datasets in a consistent fashion, more advanced algorithms that do not rely on human manipulation of individual datasets should be applied. The choice of the most suitable algorithm depends on factors such as contrast-to-noise ratio and the type and quantity of artifacts (e.g., beam hardening or ring artifacts), which are dependent on the settings and specifications of the employed scanning equipment, requiring a case-by-case evaluation. The segmentation workflow presented here relies instead on the manual determination of the intensity threshold, which is robustly applicable to any μCT data with sufficiently high contrast-to-noise ratio.

The methods used to quantify the segmented binary vascular and tubular structural data are mathematically identical to and thus a suitable replacement for manual quantification via counting frames, the gold standard in histology. They are agnostic to the means by which these binary masks were created, are therefore applicable regardless of the choice of the segmentation protocol, and can be performed entirely independent of manual user interaction in a fully automatic manner with Fiji/ImageJ.

Limitations of the Protocol

The tissue in the inner medulla did not contain detectable amounts of XlinCA despite its close proximity to the *vasa recta* through which it could have been supplied with the contrast agent. We speculate that the passive accumulation of XlinCA is specific to proximal and distal tubular cells, as other organs such as the brain did not display similar staining of tissue in our previous studies. μCT imaging of the inner medulla can be provided by other tissue staining protocols (Busse et al., 2018) that are in principle compatible with our protocol, but would require careful optimization of the different contrast levels between vascular lumen, tubular walls, and background. Incomplete tubular wall staining with XlinCA may also occur in certain pathological phenotypes that display large kidney areas fully devoid of blood vessels, since the contrast agent is distributed via the vasculature.

The presence of tubular walls as a third feature of interest besides vascular and tubular lumina reduces the signal over background for the vascular lumen alone. While the X-ray absorption values for blood vessels are well separated from the background, as can be seen in the histogram shown in Supplementary Figure S6, the related values of tissue have considerable overlap with both background and blood vessels. This results in a lower contrast-to-noise ratio, which requires either more advanced algorithms or better μCT systems to achieve vascular segmentation results comparable to methods providing vascular imaging only. Limited contrast-to-noise ratio combined with limited imaging resolution causes small features such as capillary bundles to appear as connected entities, even when they are separate in reality. Consequently, calculated path lengths as shown in Figures 4b and 4d may include, in some cases, virtual connections between adjacent vessels where, in reality, no such connections exist. The calculations should thus be seen as lower thresholds of the real path lengths. This limitation may be removed by imaging with more advanced μCT scanners.

Hard X-ray μCT can only provide structural images and cannot capture changes in protein expression or mRNA levels. Correlative microscopy is, therefore, still required for functional imaging, but limited by the high concentration of glutaraldehyde, which results in antigen masking and high autofluorescence in the kidney. The X-ray contrast agent itself has no specific fluorescence in the visible light range (Supplementary Fig. S8). The exceedingly high concentration compared with fluorescent staining nevertheless produces strong signal despite the low attenuation coefficient. However, it is only higher than background autofluorescence in the TRITC channel (Ex: 563 nm, em: 607 nm, Supplementary Fig. S9).

Conclusions

Previous approaches based on vascular casting with hydrophobic plastic resins required a large amount of optimization to avoid filling artifacts and were unable to provide both vascular and tubular structure simultaneously. This work describes a kidney preparation, image acquisition, and quantification protocol that provides full 3D imaging of these structures in whole mouse kidneys with a single procedure, and can be implemented with common imaging equipment and image processing software. The protocol greatly reduces the amount of labor and skill required for providing standard quantitative measures such as vessel density and surface areas, features fewer artifacts than vascular corrosion casting and is able to provide structural parameters inaccessible to 2D analysis such as 3D diffusion distances and path tracing.

References

Adlam D, De Bono JP, Danson EJ, Zhang MH, Casadei B, Paterson DJ & Channon KM (2011). Telemetric analysis of haemodynamic regulation during voluntary exercise training in mouse models. *Exp Physiol* **96**(11), 1118–1128.

Bankir L, Figueres L, Prot-Bertoye C, Bouby N, Crambert G, Pratt JH & Houillier P (2020). Medullary and cortical thick ascending limb: Similarities and differences. *Am J Physiol Renal Physiol* **318**(2), F422–F442.

Beeuwkes R III & Bonventre JV (1975). Tubular organization and vascular-tubular relations in the dog kidney. *Am J Physiol* **229**(3), 695–713.

Borgefors G (1996). On digital distance transforms in three dimensions. *Comput Vis Image Underst* **64**(3), 368–376.

Burgess K, Jovanovic S, Sudhir R & Jovanovic A (2019). Area under the curve analysis of blood pressure reveals increased spontaneous locomotor activity in SPAK knock-in mice: Relevance for hypotension induced by SPAK inhibition? *Physiol Rep* **7**(3), e13997.

Busse M, Muller M, Kimm MA, Ferstl S, Allner S, Achterhold K, Herzen J & Pfeiffer F (2018). Three-dimensional virtual histology enabled through cytoplasm-specific X-ray stain for microscopic and nanoscopic computed tomography. *Proc Natl Acad Sci USA* **115**(10), 2293–2298.

Chiefari J, Chong YK, Ercole F, Krstina J, Jeffery J, Le TPT, Mayadunne RTA, Meijs GF, Moad CL, Moad G, Rizzardo E & Thang SH (1998). Living free-radical polymerization by reversible addition−fragmentation chain transfer: The RAFT process. *Macromolecules* **31**(16), 5559–5562.

Chugh BP, Lerch JP, Yu LX, Pienkowski M, Harrison RV, Henkelman RM & Sled JG (2009). Measurement of cerebral blood volume in mouse brain regions using micro-computed tomography. *Neuroimage* **47**(4), 1312–1318.

Czogalla J, Schweda F & Loffing J (2016). The mouse isolated perfused kidney technique. *J Vis Exp* **117**, 54712.

Ehling J, Babickova J, Gremse F, Klinkhammer BM, Baetke S, Knuechel R, Kiessling F, Floege J, Lammers T & Boor P (2016). Quantitative micro-computed tomography imaging of vascular dysfunction in progressive kidney diseases. *J Am Soc Nephrol* **27**(2), 520–532.

Epah J, Palfi K, Dienst FL, Malacarne PF, Bremer R, Salamon M, Kumar S, Jo H, Schurmann C & Brandes RP (2018). 3D Imaging and quantitative analysis of vascular networks: A comparison of ultramicroscopy and micro-computed tomography. *Theranostics* **8**(8), 2117–2133.

Fan L, Wang S, He X, Gonzalez-Fernandez E, Lechene C, Fan F & Roman RJ (2019). Visualization of the intrarenal distribution of capillary blood flow. *Physiol Rep* **7**(8), e14065.

Garcia-Sanz A, Rodriguez-Barbero A, Bentley MD, Ritman EL & Romero JC (1998). Three-dimensional microcomputed tomography of renal vasculature in rats. *Hypertension* **31**(1 Pt 2), 440–444.

Gardiner BS, Smith DW, O'Connor PM & Evans RG (2011). A mathematical model of diffusional shunting of oxygen from arteries to veins in the kidney. *Am J Physiol Renal Physiol* **300**(6), F1339–F1352.

Ghanavati S, Yu LX, Lerch JP & Sled JG (2014). A perfusion procedure for imaging of the mouse cerebral vasculature by X-ray micro-CT. *J Neurosci Methods* **221**, 70–77.

Grabherr S, Djonov V, Yen K, Thali MJ & Dirnhofer R (2007). Postmortem angiography: Review of former and current methods. *AJR Am J Roentgenol* **188**(3), 832–838.

Grabherr S, Hess A, Karolczak M, Thali MJ, Friess SD, Kalender WA, Dirnhofer R & Djonov V (2008). Angiofil-mediated visualization of the vascular system by microcomputed tomography: A feasibility study. *Microsc Res Technol* **71**(7), 551–556.

Haenssgen K, Makanya AN & Djonov V (2014). Casting materials and their application in research and teaching. *Microsc Microanal* **20**(2), 493–513.

Hall AM, Rhodes GJ, Sandoval RM, Corridon PR & Molitoris BA (2013). *In vivo* multiphoton imaging of mitochondrial structure and function during acute kidney injury. *Kidney Int* **83**(1), 72–83.

Hlushchuk R, Zubler C, Barre S, Correa Shokiche C, Schaad L, Rothlisberger R, Wnuk M, Daniel C, Khoma O, Tschanz SA, Reyes M & Djonov V (2018). Cutting-edge microangio-CT: New dimensions in vascular imaging and kidney morphometry. *Am J Physiol Renal Physiol* **314**(3), F493–F499.

Hossler FE & Douglas JE (2001). Vascular corrosion casting: Review of advantages and limitations in the application of some simple quantitative methods. *Microsc Microanal* **7**(3), 253–264.

Hossler FE, Lametschwandtner A, Kao R & Finsterbusch F (2013). Microvascular architecture of mouse urinary bladder described with vascular corrosion casting, light microscopy, SEM, and TEM. *Microsc Microanal* **19**(6), 1428–1435.

Hyde DM, Tyler NK & Plopper CG (2007). Morphometry of the respiratory tract: Avoiding the sampling, size, orientation, and reference traps. *Toxicol Pathol* **35**(1), 41–48.

Jin E & Lu ZR (2014). Biodegradable iodinated polydisulfides as contrast agents for CT angiography. *Biomaterials* **35**(22), 5822–5829.

Klingberg A, Hasenberg A, Ludwig-Portugall I, Medyukhina A, Mann L, Brenzel A, Engel DR, Figge MT, Kurts C & Gunzer M (2017). Fully automated evaluation of total glomerular number and capillary tuft size in nephritic kidneys using lightsheet microscopy. *J Am Soc Nephrol* **28**(2), 452–459.

Kolesova H, Capek M, Radochova B, Janacek J & Sedmera D (2016). Comparison of different tissue clearing methods and 3D imaging techniques for visualization of GFP-expressing mouse embryos and embryonic hearts. *Histochem Cell Biol* **146**(2), 141–152.

Kriz W (1981). Structural organization of the renal medulla: Comparative and functional aspects. *Am J Physiol* **241**(1), R3–R16.

Krucker T, Lang A & Meyer EP (2006). New polyurethane-based material for vascular corrosion casting with improved physical and imaging characteristics. *Microsc Res Technol* **69**(2), 138–147.

Kuo W & Kurtcuoglu V (2017). Renal arteriovenous oxygen shunting. *Curr Opin Nephrol Hypertens* **26**(4), 290–295.

Lai JT, Filla D & Shea R (2002). Functional polymers from novel carboxyl-terminated trithiocarbonates as highly efficient RAFT agents. *Macromolecules* **35**(18), 6754–6756.

Lantuejoul C & Beucher S (1981). On the use of the geodesic metric in image-analysis. *J Microsc* **121**, 39–49.

Le NA, Kuo W, Müller B, Kurtcuoglu V & Spingler B (2020). Crosslinkable polymeric contrast agent for high-resolution X-ray imaging of the vascular system. *Chem Commun* **56**(44), 5885–5888.

Legland D, Arganda-Carreras I & Andrey P (2016). MorphoLibJ: Integrated library and plugins for mathematical morphology with ImageJ. *Bioinformatics* **32**(22), 3532–3534.

Lusic H & Grinstaff MW (2013). X-ray-computed tomography contrast agents. *Chem Rev* **113**(3), 1641–1666.

Ngo JP, Kar S, Kett MM, Gardiner BS, Pearson JT, Smith DW, Ludbrook J, Bertram JF & Evans RG (2014). Vascular geometry and oxygen diffusion in the vicinity of artery–vein pairs in the kidney. *Am J Physiol Renal Physiol* **307**(10), F1111–F1122.

Nordsletten DA, Blackett S, Bentley MD, Ritman EL & Smith NP (2006). Structural morphology of renal vasculature. *Am J Physiol Heart Circ Physiol* **291**(1), H296–H309.

Olgac U & Kurtcuoglu V (2015). Renal oxygenation: Preglomerular vasculature is an unlikely contributor to renal oxygen shunting. *Am J Physiol Renal Physiol* **308**(7), F671–F688.

Olgac U & Kurtcuoglu V (2016). The Bohr effect is not a likely promoter of renal preglomerular oxygen shunting. *Front Physiol* **7**, 482.

Ollion J, Cochennec J, Loll F, Escude C & Boudier T (2013). TANGO: A generic tool for high-throughput 3D image analysis for studying nuclear organization. *Bioinformatics* **29**(14), 1840–1841.

Ortiz MC, Garcia-Sanz A, Bentley MD, Fortepiani LA, Garcia-Estan J, Ritman EL, Romero JC & Juncos LA (2000). Microcomputed tomography of kidneys following chronic bile duct ligation. *Kidney Int* **58**(4), 1632–1640.

Pallone TL, Zhang Z & Rhinehart K (2003). Physiology of the renal medullary microcirculation. *Am J Physiol Renal Physiol* **284**(2), F253–F266.

Perrien DS, Saleh MA, Takahashi K, Madhur MS, Harrison DG, Harris RC & Takahashi T (2016). Novel methods for microCT-based analyses of vasculature in the renal cortex reveal a loss of perfusable arterioles and glomeruli in eNOS−/− mice. *BMC Nephrol* **17**, 24.

Prommer HU, Maurer J, von Websky K, Freise C, Sommer K, Nasser H, Samapati R, Reglin B, Guimaraes P, Pries AR & Querfeld U (2018). Chronic kidney disease induces a systemic microangiopathy, tissue hypoxia and dysfunctional angiogenesis. *Sci Rep* **8**(1), 5317.

Richardson DS & Lichtman JW (2015). Clarifying tissue clearing. *Cell* **162**(2), 246–257.

Roberts N, Magee D, Song Y, Brabazon K, Shires M, Crellin D, Orsi NM, Quirke R, Quirke P & Treanor D (2012). Toward routine use of 3D histopathology as a research tool. *Am J Pathol* **180**(5), 1835–1842.

Schindelin J, Arganda-Carreras I, Frise E, Kaynig V, Longair M, Pietzsch T, Preibisch S, Rueden C, Saalfeld S, Schmid B, Tinevez JY, White DJ, Hartenstein V, Eliceiri K, Tomancak P & Cardona A (2012). Fiji: An open-source platform for biological-image analysis. *Nat Methods* **9**(7), 676–682.

Schneider CA, Rasband WS & Eliceiri KW (2012). NIH Image to ImageJ: 25 years of image analysis. *Nat Methods* **9**(7), 671–675.

Stowell RE (2009). Effect on tissue volume of various methods of fixation, dehydration, and embedding. *Stain Technol* **16**(2), 67–83.

Tanaka T & Nangaku M (2013). Angiogenesis and hypoxia in the kidney. *Nat Rev Nephrol* **9**(4), 211–222.

Tran T, Sundaram CP, Bahler CD, Eble JN, Grignon DJ, Monn MF, Simper NB & Cheng L (2015). Correcting the shrinkage effects of formalin fixation and tissue processing for renal tumors: Toward standardization of pathological reporting of tumor size. *J Cancer* **6**(8), 759–766.

Vasquez SX, Gao F, Su F, Grijalva V, Pope J, Martin B, Stinstra J, Masner M, Shah N, Weinstein DM, Farias-Eisner R & Reddy ST (2011). Optimization of microCT imaging and blood vessel diameter quantitation of preclinical specimen vasculature with radiopaque polymer injection medium. *PLoS One* **6**(4), e19099.

Venkatachalam MA, Weinberg JM, Kriz W & Bidani AK (2015). Failed tubule recovery, AKI-CKD transition, and kidney disease progression. *J Am Soc Nephrol* **26**(8), 1765–1776.

Wagner R, Van Loo D, Hossler F, Czymmek K, Pauwels E & Van Hoorebeke L (2011). High-resolution imaging of kidney vascular corrosion casts with Nano-CT. *Microsc Microanal* **17**(2), 215–219.

Wagner RC, Czymmek K & Hossler FE (2006). Confocal microscopy, computer modeling, and quantification of glomerular vascular corrosion casts. *Microsc Microanal* **12**(3), 262–268.

Wei W, Popov V, Walocha JA, Wen J & Bello-Reuss E (2006). Evidence of angiogenesis and microvascular regression in autosomal-dominant polycystic kidney disease kidneys: A corrosion cast study. *Kidney Int* **70**(7), 1261–1268.

Yang B, Treweek JB, Kulkarni RP, Deverman BE, Chen CK, Lubeck E, Shah S, Cai L & Gradinaru V (2014). Single-cell phenotyping within transparent intact tissue through whole-body clearing. *Cell* **158**(4), 945–958.

Zhai XY, Thomsen JS, Birn H, Kristoffersen IB, Andreasen A & Christensen EI (2006). Three-dimensional reconstruction of the mouse nephron. *J Am Soc Nephrol* **17**(1), 77–88.